Critical Role of Disorder for Superconductivity in the Series of Epitaxial Ti(O,N) Films

Authors: Fengmiao Li^{1,2}, Oliver Dicks², Myung-Geun Han³, Solveig Aamlid², Giorgio Levy^{1,2}, Ronny Sutarto⁴, Chong Liu^{1,2}, Hsiang-Hsi Kung^{1,2}, Oleksandr Foyevstov^{1,2}, Simon Godin^{1,2}, Bruce A. Davidson^{1,2}, Andrea Damascelli^{1,2}, Yimei Zhu³, Christoph Heil⁵, Ilya Elfimov^{1,2}, George A. Sawatzky^{1,2}, Ke Zou^{1,2}

Affiliations:

¹Department of Physics & Astronomy, University of British Columbia, Vancouver, British Columbia, V6T 1Z1 Canada.

²Quantum Matter Institute, University of British Columbia, Vancouver, British Columbia, V6T 1Z4 Canada.

³Condensed Matter Physics & Materials Science Department, Brookhaven National Laboratory, Upton, New York, 11973 USA.

⁴Canadian Light Source, Saskatoon, Saskatchewan, S7N 2V3 Canada.

⁵Institute of Theoretical and Computational Physics, Graz University of Technology, NAWI Graz, 8010 Graz, Austria

Abstract: Experimental manipulation of superconductivity is of paramount importance, not only for practical applications but also for identifying the key factors involved in electron pairing. In this work, we have undertaken a meticulous study of the superconductivity in a series of titanium compounds with a rocksalt structure, synthesized as epitaxial films. We find that substituting nitrogen (N) for oxygen (O) in titanium monoxide (TiO) with the stoichiometry close to

 $TiO_{0.6}N_{0.4}$ leads to superconductivity with a transition temperature (T_c) of ~2.6 K, about five times higher than that of TiO at ~0.5 K and half as high as the T_c of ~6 K in titanium nitride (TiN). However, Eliashberg theoretical calculations predict similar T_c in TiO, Ti oxynitride and TiN. The analysis of electron mean free path suggests the presence of significant disorder in TiO and a remarkable reduction in the impact of disorder in oxynitrides. Density functional theory (DFT) calculations reveal that disorder decreases the coherence of electronic states for non-zero momenta, which would degrade the influence of electron-phonon. Our findings demonstrate the disorder and superconductivity depend strongly on the N/O ratio, highlighting the critical role of disorder for superconductivity in this series of Ti(O,N) materials.

Introduction:

The Bardeen–Cooper–Schrieffer (BCS) theory, which requires bosons such as phonons and magnons as the medium for pairing two distant electrons, serves as one of the prevailing microscopic mechanisms for superconductivity ¹. Superconductivity is observed in many metal oxides as the result of electron-phonon coupling, including K-doped BaBiO₃ ², electron-doped SrTiO₃ ³, LaO ⁴, NbO ⁵, and SnO ⁶. However, superconductivity in many transition-metal oxides, including cuprates ⁷ and recently revisited nickelates ⁸, is unconventional due to quantum many-body effects derived from intricate electron correlations and magnetic interactions. In the normal state, unconventional superconductors like cuprates ⁹ and nickelates ⁸ are "strange" or "bad" metals with the mean free path of electron scattering shorter than the nearest atom distance, hinting at the existence of significant scattering centers ¹⁰. In fact, most of these materials have almost perfect crystal structures after years' efforts on optimizing the crystal growth, indicating that the short-range electron scattering arises from some intrinsic mechanism distinctive from crystal defects or impurities. Additionally, chemical substitution, which is crucial for creating

superconductivity states in many of these materials, introduces an irregular Coulomb potential with the interaction range usually much larger than the interaction distances.

According to Anderson's theorem, conventional superconductors with formed bosonic Cooper pairs with zero center of mass momentum are not vulnerable to nonmagnetic impurities ¹¹. The potential influence of disorder in the process of forming electron pairings has been investigated intensively ^{11–13} but the disorder effect dependent on the studied system remains elusive possibly due to the complexity created by its interactions with other degrees of freedom, such as charge and spin In the search for suitable systems for the study of disorder-superconductivity relation, it is perceived that the recently discovered superconductor, rocksalt TiO, with a T_c ~0.5 K has a mean free path shorter than the nearest atom distance ¹⁴, reminiscent of the "bad" metal characteristics in high-T_c superconductors ¹⁰; Rock-salt TiN, an isostructural material of TiO, exhibits one order of magnitude higher superconducting T_c at ~6 K and a much longer elastic scattering length ¹⁵. Owing to relatively simplified electronic structures and less complexity from spin and charge degrees of freedom, this series of materials from TiO to TiN thus provides an ideal platform for the study of disorder effects on superconductivity.

Through meticulous experimental and theoretical investigations, we have delved into the fundamental mechanisms that govern the coherence of electron wavefunctions, shaping the superconductivity in the Ti(N,O) series. In this study, we employed molecular beam epitaxy (MBE) to successfully synthesize an intermediate phase of TiO and TiN, known as Ti oxynitride films. Our results show that N substitution for O in TiO strongly enhances superconductivity and increases the electron mean free path in the normal state, in spite of anion intermixing. The gradual chemical substitution of O increases disorder in anion sublattice but decreases the

original disorder caused by inherent instability in TiO, resulting in an interplay of these two types of disorder that affects superconductivity.

Ti oxynitride film growth, structure, and stoichiometry. To prepare titanium oxynitride films, state-of-the-art MBE 16,17 is used where Ti deposition on single-crystal MgO occurs in a nitric oxide (NO) gaseous environment. The MgO (001) substrate is chosen because of its rocksalt structure and a near perfect lattice match to TiO and TiN. The NO gas serves as oxidizing agent and source for both N and O. Multiple reciprocal- and real-space techniques were used to characterize prepared Ti oxynitride films. *In situ* reflection high-energy electron diffraction (RHEED) and low-energy electron diffraction (LEED) (shown in Fig. 1A-C) with bright specular reflection and sharp diffraction spots revealed highly-ordered and smooth film surfaces. Reciprocal space mapping (RSM) (Fig. 1D) from x-ray diffraction (XRD) demonstrates that the coherent film growth is maintained up to a thickness of ~90 nm. XRD 2θ-ω scan (Fig. 1E) shows a single and sharp (002) diffraction peak from the film with no apparent phase separation into TiO and TiN. The out-of-plane lattice constant is calculated to be ~4.23 Å, which falls within the range of the values of TiO 14 and TiN films epitaxially grown on MgO(001) substrates 14,15 .

The Ti and Mg atom columns in the rock-salt lattice are resolved in the high-angle annular dark-field (HAADF) scanning transmission electron microscopy (STEM) image (Fig. 1F). The annular bright field (ABF) STEM (Fig. 1G) sensitive to the light element probes the anion atom in the film and the substrate. The element-specific electron energy loss spectra (EELS) (Fig. 1H) in STEM at the Ti L_{2,3}, N K, and O K edges confirm the presence of Ti, N and O, consistent with our results from x-ray absorption and photoemission spectroscopy experiments (XAS & XPS, Fig. S1 & S2). The ratio of Ti, O and N elements, which is obtained

from the area intensity of EELS at different element x-ray absorption edges divided by electron-excitation cross section factors, is found to be approximately 10:6:4 with a $\sim\pm10\%$ error bar, *i.e.* $TiO_{0.6}N_{0.4}$. NO gas naturally supplies an equal number of N and O atoms for the sample growth; the higher reactivity of oxygen to Ti results in the disproportionation of N and O concentration in prepared films. We have reproduced the same N and O ratio in multiple samples, showing a thermodynamically-stable synthesis. It is worth noting that N and O are distributed in a random fashion at anion sites since no atomic order was detected in STEM and XRD.

Electrical transport properties and superconductivity. Despite N and O mixing, $TiO_{0.6}N_{0.4}$ films have a lower normal-state resistivity of ~100 μΩ·cm than TiO films at ~300 μΩ·cm. The resistivity of the $TiO_{0.6}N_{0.4}$ film exhibits weak temperature dependence with a positive derivative when the sample is cooled down, in contrast to the small negative slope observed in the resistivity (ρ_{xx}) versus temperature (T) measurement of TiO ¹⁴. In this regard, N doping has transformed TiO from a "bad" metal to a metallic-like temperature dependence. The electron mean free paths for TiO, $TiO_{0.6}N_{0.4}$ and TiN are, respectively, ~2 Å ¹⁴, ~6 Å, and ~1000 Å ¹⁵ at low temperatures just above the T_c , which are calculated from the measured resistivity (Fig. 4A) and the Drude model, three-dimensional free electron gas model ¹⁸. As shown in Fig. 2B, the Hall measurement reveals that the free carrier is electron-type, and the carrier density around 8.0 × 10^{22} cm⁻³ slightly decreases at lower temperatures.

Remarkably, we observe a superconducting transition with a $T_c \sim 2.6$ K, as shown in the inset of Fig. 2A. The decreasing T_c with applied out-of-the-pane magnetic field (Figure 2C) demonstrates that the superconductivity is suppressed. The upper critical field H_{c2} (T) in Fig. 2D is obtained from the 50% criterion of the normal state resistance value in Fig. 2C. The excellent fit to the Werthamer-Helfand-Hohenberg (WHH) model ¹⁹ yields the H_{c2} (0) of ~ 1.4 T. At 0 K,

the superconducting Landau-Ginzburg superconducting coherence length is equal to $\xi = [(h/2e)/(2\pi H_{c2})]^{1/2} \approx 16$ nm. The electron mean free path in the normal state (i.e., ~ 0.6 nm) is considerably shorter than the superconducting coherent length, leaving Ti oxynitrides in the "dirty" regime of superconductors.

Electronic structures of Ti oxynitride films. Our current study together with previous research in superconductivity on TiO 14 and TiN 15 shows that the T_c as well as electron mean free path increase from TiO, TiO_{0.6}N_{0.4} to TiN. The possible origin of electron scattering and its influence on the band structure dispersion will be discussed.

To investigate the low-energy electronic structures, we utilized complementary experimental and theoretical methods, including ultraviolet photoemission spectroscopy (UPS), soft x-ray absorption spectroscopy (XAS) and density functional theory (DFT). The UPS was used to measure occupied valence states, and the resulting metallic property of Ti oxynitride films is confirmed by the abrupt cutoff at the Fermi energy set to zero shown in Fig. 3A. The calculated spectrum in Fig. 3B shows that the states near the Fermi level are primarily Ti 3d t_{2g} and the spectral weight at higher binding energies is due to the excitation of O and N 2p occupied states.

The nitrogen XAS at the K edge corresponds to electron excitation from the core-level 1s orbital to unoccupied 2p states. The experimental data is interpreted using projected N p states from DFT calculations, with separation of the two peaks at ~397.9 eV and ~400 eV originating from the splitting of the Ti 3d t_{2g} and e_g states due to crystal and ligand field effects. The peaks at higher energies are due to the excitation of electrons to empty N 2p states hybridizing with Ti 4s and 4p bands. Notably, the additional shoulder at ~397.1 eV, corresponding to the small bump in the projected DOS in Fig. 3D, results from the mixture of N and O at anionic sites. Interestingly,

XAS at the O (Fig. S2) and N K edge are similar to those obtained from TiN and TiO ^{14,20}, implying that Ti-O and Ti-N bonding in oxynitrides resembles those in TiO and TiN. The Ti XAS at the L_{2,3} edge (Fig. S2) features two broad primary peaks with pronounced additional peaks at lower energies that possibly originate from the nominal Ti valence between 2+ and 3+. The excellent agreement between experimental results and theoretical calculations demonstrates that the electronic structure of Ti oxynitrides is in close proximity to the non-spin polarized solution predicted by DFT.

Theoretical considerations suggest TiO should have a higher T_c than TiN. Naively, in the weak coupling theory of superconductivity, T_c is proportional to the phonon frequency and the increase of the density of states near the Fermi energy ²¹. Our DFT calculations show TiO has a higher total density of states at the Fermi level than TiN (Fig. 4B), whilst having phonon frequencies of similar magnitude. Solving the semi-empirical Allen-Dynes McMillan formula gives a T_c of about 12 K for TiO and about 9 K for TiN and more precise calculations of the superconducting properties employing the Eliashberg equations as implemented in the EPW code ²² predict TiO to have a T_c in the range of 15-16 K, even larger than TiN (14-15 K). This remarkable discrepancy between theory and experiment in T_c strongly suggests other interactions must play a nonnegligible role.

In the following, we will examine the band dispersion using DFT that includes the effect of disorder. As N content is increased from oxides to nitrides, the band dispersion of the Ti t_{2g} bands at energies between 2 eV and -4 eV shows large similarities (Fig. 4C-E) but with some differences due to the differential bonding of Ti to N and O. One notable change upon N doping is that the Fermi level that crosses Ti t_{2g} bands moves lower in energy because of the more negative N valence, namely a nominal valence of 3-. The excellent agreement between DFT and

experimental XAS supports that N substitution for O indeed dopes holes into the system ^{16,17}. The very short electron mean free path in TiO reveals it is a "dirty" system with a high density of scattering centers. In the substrate-assisted epitaxial TiO films, the number of defects is minimized due to epitaxial stabilization from the defect-free substrate template ¹⁴. This suggests the disorder originates from the intrinsic instability of TiO which is known to host both O and Ti vacancies in the bulk with a tendency to retain stoichiometry of 1/1, similar to other binary monoxides such as NbO ²³. In these films, however, the vacancies seem not to be ordered, otherwise it would be visible in the structural studies performed. It therefore becomes clear that the electronic structure (as shown in Fig. 4C) calculated using a primitive unitcell without disorder does not accurately reflect the true nature of TiO.

The unfolded band structure (Fig. 4D) of a supercell (64 Ti, 39 O and 25 N giving the nominal stoichiometry TiO_{0.61}N_{0.39}) with quasi-randomly distributed N and O (see Fig. S3 and the methods section for structure generation and band unfolding procedure) shows that the Ti t_{2g} and anion (N & O) 2p band dispersion off the Brillouin Zone (BZ) center is largely smeared out due to the disordered potential, which stems from lattice distortion induced by the O and N mixture and the strongly different scattering potentials exhibited by negatively trivalent N as compared to negatively divalent O. Interestingly, the coherence of electronic states close to the BZ center is preserved because, in a long-range domain, the disorder effect is averaged out and not visible for long-wavelength electrons. Momentum-dependent broadening of phonon dispersion is also seen in the phonon calculation of Ti oxynitrides (Fig. S4). Although the disorder in TiO may originate from lattice and /or charge -derived scattering due to the above mentioned O and Ti vacancies, the disorder effect, introducing decoherence at non-zero momenta of electronic states, is similar. In contrast, TiN, a "clean" system with a very long

electron mean path, possesses electronic states without disorder-induced decoherence in close proximity to the states predicted by DFT (as shown in Fig. 4E).

Discussions. The disorder-induced decoherence in TiO results in the weakened electronphonon coupling; in TiN, the electronic states throughout the Brillouin zone retain their
coherence, which leads to a higher T_c. TiO_{0.6}N_{0.4} although carrying extra anion intermixing, is
less disordered than TiO because of N stabilization, therefore, exhibiting an intermediate T_c.
Although rocksalt Ti compounds exhibit the nature closely resembling the scenario described by
single-particle physics, the presence of fluctuating local magnetic moment originating from
electron correlation cannot be excluded. Nitrides typically exhibit weaker electron correlation
compared to oxides due to stronger screening effect; the influence of local magnetic fluctuation
on superconductivity T_c and electron scattering in the normal state in TiO requires further
studies. Our experimental and theoretical results demonstrate that the disorder plays an important
role in the process of forming Cooper pairs and decreases the superconducting transition
temperature in this series of Ti-based superconducting compounds.

Concluding remarks. In this study, we have discovered that the MBE-grown $TiO_{0.6}N_{0.4}$ epitaxial film, an intermediate phase of TiO and TiN, exhibits superconductivity with $T_c \sim 2.6$ K. Disorder in TiO effectively reduces the coherence of the system, with the exception of those electronic states located in close proximity to the center of the Brillouin zone. Substituting N for O shifts the Fermi level, changes the shape of Fermi surface and, more importantly, decreases the amount of disorder evidenced by electrical transport measurements, increasing the coherence of electronic states in the systems. Our results demonstrate that momentum dependent decoherence caused by the disorder should be considered in the quantitative study of underlying mechanism for superconductivity in $TiO_{1-x}N_x$ and other superconductors.

Methods

MBE film growth: The MgO (001) substrate was annealed at 700 °C in ultra-high vacuum (UHV) for 1 hour before the film growth. In order to maintain the growth of high-quality films, the NO pressure in the growth chamber was kept at $\sim 1.0 \times 10^{-8}$ Torr within a small pressure variation window by adjusting a leak valve and the growth rate was at ~ 1 layer/min, as determined by the Ti flux measured by a quartz crystal microbalance (QCM). A higher or lower NO growth pressure causes undesired phases, such as Ti_2O_3 and Ti metal. A protective layer of Germanium (Ge) film with a thickness of ~ 40 nm is deposited at room temperature for *ex-situ* measurements.

<u>Transport measurement</u>: Temperature-dependent resistivity from 300 K to 2 K were performed with Van der Pauw geometry in a Quantum Design physical property measurement system (PPMS). Indium metal was used as the contact electrode.

<u>X-ray diffraction measurement</u>: The 90 nm film with a Ge capping layer was measured using x-ray single crystal diffractometer, Bruker D8 DISCOVER at the room temperature.

Spectroscopy measurement: Room-temperature UPS measurement was done at the UBC ARPES lab. A vacuum suitcase with better than 1×10^{-11} Torr vacuum was used for transferring samples from the MBE growth chamber to the characterization chamber. The photon energy is at 21.2 eV. Fluorescence yield of XAS was collected at 10° angle away from the sample surface with the incoming x-ray beam at 30° angle relative to the sample surface. *Ex-situ* XAS and XPS measurements were performed at Resonant Elastic and Inelastic X-Ray Scattering (REIXS) beamline of Canadian Light Source. The XPS Al x-ray source was monochromatized at 1486.6 eV with an energy resolution of \sim 0.4 eV at the Fermi level of Ag.

STEM experiments: For STEM, Ge-capped Ti oxynitride films on MgO (001) substrates were cross-sectioned by focused ion beam technique using 5 keV Ga+ ions to minimize ion beam-induced damages. A JEOL ARM 200CF equipped with a cold field emission gun and double spherical aberration correction at Brookhaven National Laboratory operated at 200 kV was used for HAADF imaging with detection angles ranging from 68 to 280 mrad. For EELS, a Gatan Quantum ER spectrometer was used with dispersion (0.1 eV/channel) and ~0.8 eV energy resolution. The convergent and collection semiangles were, respectively, ~10 and ~5 mrad.

DFT calculations: Density functional theory calculations were performed within the Projector Augmented Wave method²⁴ and the Perdew-Burke-Ernzerhof functional²⁵, as implemented in the Quantum Espresso package^{26,27}. The disordered supercell for Ti oxynitride calculations was made using the mcsqs code from the Alloy Theoretic Automated Toolkit (ATAT) ²⁸. The code uses a Monte Carlo algorithm to generate Special Quasi-random Structures (SQS). For the SQS cell, a supercell (4×4×4 of the primitive unitcell) with 25 N atoms and 39 O atoms was initialized (Fig. S3), and the correlations of anion pairs up to 6 Å, triples up to 3 Å, and quadruples up to 3 Å were optimized until the correlation mismatch was less than 0.01 for all clusters. The supercell band structure was unfolded using the unfold.x code ²⁹. Crystal structures were plotted using the VESTA software ³⁰.

We employed the EPW code package^{31–34} for the Wannier interpolation of the electron-phonon matrix elements onto dense k- and q-grids and the subsequent self-consistent solution of the isotropic Migdal-Eliashberg equations. In particular, we used coarse $6\times6\times6$ k- and q-grids and interpolated onto fine $24\times24\times24$ reciprocal grids, set a Matsubara frequency cutoff of 1eV, included electronic states within ±1 eV around the Fermi energy, and chose a standard value for the Morel-Anderson pseudopotential of mu*=0.10. In a stoichiometric and primitive unitcell

TiO, where imaginary phonon frequencies ³⁵ appear when performing phonon calculations in the harmonic approximation, all electron-phonon matrix elements corresponding to such harmonically unstable phonon modes have been set to zero.

Acknowledgements

This research was undertaken thanks in part to funding from the Max Planck-UBC-UTokyo Centre for Quantum Materials and the Canada First Research Excellence Fund, Quantum Materials and Future Technologies Program. The work at UBC was also supported by the Natural Sciences and Engineering Research Council of Canada (NSERC), British Columbia Knowledge Development fund (BCKDF), Canada Foundation for Innovation (CFI), Canada Research Chair Program (A.D.), and CIFAR Quantum Materials Program (A.D.). XAS and XPS characterizations were performed at the Canadian Light Source, a national research facility of University of Saskatchewan, which is supported by CFI, NSERC, the National Research Council (NRC), the Canadian Institutes of Health Research (CIHR), the Government of Saskatchewan, and the University of Saskatchewan. The STEM work at the Brookhaven National Laboratory was supported by the U.S. DOE Basic Energy Sciences, Materials Science and Engineering Division under Contract No. DESC0012704. This research used the focused ion beam instrument at the Center for Functional Nanomaterials, a U.S. Department of Energy Office of Science User Facility, at the Brookhaven National Laboratory. C.H. and O.D. were financially supported by Intellectual Ventures - Deep Science Fund. C.H. also acknowledges the Austrian Science Fund (FWF) Project No. P 32144-N36.

References and Notes:

1. Taylor, A. W. B. The microscopic theory of superconductivity. *Contemp. Phys.* **9**, 549–564 (1968).

- 2. Cava, R. J. *et al.* Superconductivity near 30 K without copper: the Ba0. 6K0. 4BiO3 perovskite. *Nature* **332**, 814–816 (1988).
- 3. Schooley, J. F., Hosler, W. R. & Cohen, M. L. Superconductivity in Semiconducting SrTiO3. *Phys. Rev. Lett.* **12**, 474–475 (1964).
- 4. Kaminaga, K., Oka, D., Hasegawa, T. & Fukumura, T. Superconductivity of Rock-Salt Structure LaO Epitaxial Thin Film. *J. Am. Chem. Soc.* **140**, 6754–6757 (2018).
- 5. Hulm, J. K., Jones, C. K., Hein, R. A. & Gibson, J. W. Superconductivity in the TiO and NbO systems. *J. Low Temp. Phys.* **7**, 291–307 (1972).
- 6. Forthaus, M. K. *et al.* Superconductivity in SnO: A nonmagnetic analog to Fe-based superconductors? *Phys. Rev. Lett.* **105**, 1–4 (2010).
- 7. Keimer, B., Kivelson, S. A., Norman, M. R., Uchida, S. & Zaanen, J. From quantum matter to high-temperature superconductivity in copper oxides. *Nature* **518**, 179–186 (2015).
- 8. Li, D. et al. Superconductivity in an infinite-layer nickelate. Nature 572, 624–627 (2019).
- 9. Bednorz, J. G. & Müller, K. A. Possible high T_c superconductivity in the Ba-La-Cu-O system. *Zeitschrift für Phys. B Condens. Matter* **64**, 189–193 (1986).
- 10. Hussey, N. E., Takenaka, K. & Takagi, H. Universality of the Mott-Ioffe-Regel limit in metals. *Philos. Mag.* **84**, 2847–2864 (2004).
- 11. Anderson, P. W. Theory of dirty superconductors. *Career Theor. Physics, A (2nd Ed.* II, 114–118 (2005).
- 12. Gastiasoro, M. N. & Andersen, B. M. Enhancing superconductivity by disorder. Phys.

- Rev. B 98, 1-6 (2018).
- 13. Mackenzie, A. P. *et al.* Extremely Strong Dependence of Superconductivity on Disorder in Sr2RuO4. *Phys. Rev. Lett.* **80**, 161–164 (1998).
- 14. Li, F. *et al.* Single-crystalline epitaxial TiO film: A metal and superconductor, similar to Ti metal. *Sci. Adv.* 7, 1–8 (2021).
- 15. Krockenberger, Y., Karimoto, S. I., Yamamoto, H. & Semba, K. Coherent growth of superconducting TiN thin films by plasma enhanced molecular beam epitaxy. *J. Appl. Phys.* **112**, 1–5 (2012).
- 16. Wicks, R. et al. NO-assisted molecular-beam epitaxial growth of nitrogen substituted EuO. Appl. Phys. Lett. 100, 162405 (2012).
- 17. Elfimov, I. S. *et al.* Magnetizing oxides by substituting nitrogen for oxygen. *Phys. Rev. Lett.* **98**, 2–5 (2007).
- 18. Gunnarsson, O., Calandra, M. & Han, J. E. Colloquium: Saturation of electrical resistivity.

 *Rev. Mod. Phys. 75, 1085–1099 (2003).
- 19. Werthamer, N. R., Helfand, E. & Hohenberg, P. C. Temperature and purity dependence of the superconducting critical field, H_{c2}. III. electron spin and spin-orbit effects. *Phys. Rev.* **147**, 295–302 (1966).
- Rattanachai, Y., Rintramee, K., Rattanasuporn, S. & Supruangnet, R. Characterization of Nafion XL membrane for PEMFC after VUV degradation and titanium nitride coating. Nucl. Instruments Methods Phys. Res. Sect. B Beam Interact. with Mater. Atoms 436, 292–297 (2018).
- 21. Carbotte, J. P. Properties of boson-exchange superconductors. Rev. Mod. Phys. 62, 1027-

- 1157 (1990).
- Ponce, S., Margine, E. R., Verdi, C. & Giustino, F. EPW: Electron–phonon coupling, transport and superconducting properties using maximally localized Wannier functions. *Comput. Phys. Commun.* 209, 116–133 (2016).
- 23. Efimenko, A. K. *et al.* Electronic signature of the vacancy ordering in NbO (Nb 3 O 3). **195112**, 1–7 (2017).
- 24. Blöchl, P. E. Projector augmented-wave method. *Phys. Rev. B* **50**, 17953 (1994).
- 25. Perdew, J. P., Burke, K. & Ernzerhof, M. Generalized gradient approximation made simple. *Phys. Rev. Lett.* 77, 3865–3868 (1996).
- 26. Giannozzi, P. *et al.* QUANTUM ESPRESSO: a modular and open-source software project for quantum simulations of materials. *J. Phys. Condens. matter* **21**, 395502 (2009).
- 27. Giannozzi, P. et al. Advanced capabilities for materials modelling with Quantum ESPRESSO. J. Phys. Condens. matter 29, 465901 (2017).
- 28. de Walle, A. *et al.* Efficient stochastic generation of special quasirandom structures. *Calphad* **42**, 13–18 (2013).
- 29. Popescu, V. & Zunger, A. Extracting E versus k effective band structure from supercell calculations on alloys and impurities. *Phys. Rev. B* **85**, 85201 (2012).
- 30. Momma, K. & Izumi, F. VESTA 3 for three-dimensional visualization of crystal, volumetric and morphology data. *J. Appl. Crystallogr.* **44**, 1272–1276 (2011).
- 31. Margine, E. R. & Giustino, F. Anisotropic migdal-eliashberg theory using wannier functions. *Phys. Rev. B* **87**, 24505 (2013).

- 32. Ponce, S., Margine, E. R., Verdi, C. & Giustino, F. EPW: Electron--phonon coupling, transport and superconducting properties using maximally localized Wannier functions. *Comput. Phys. Commun.* **209**, 116–133 (2016).
- 33. Martín González, M. S. et al. In situ reduction of (100) SrTiO3. Solid State Sci. 2, 519–524 (2000).
- 34. Lee, H. *et al.* Electron-phonon physics from first principles using the EPW code. *arXiv Prepr. arXiv2302.08085* (2023).
- 35. Hosseini, S. V., Abbasnejad, M. & Mohammadizadeh, M. R. Influence of vacancies on phonons and pressure phase transitions in TiO: a DFT study. *arXiv Prepr. arXiv2110.12267* (2021).

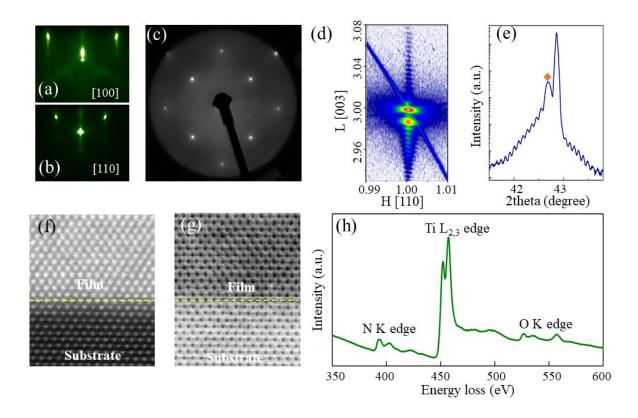


Fig. 1. High-quality titanium oxynitride epitaxial films synthesized using MBE. (a) and (b) show RHEED patterns of a 90 nm film surface with the incident beam along [100] and [110] direction, respectively. (c) the LEED pattern of the film surface collected using a 180 eV electron beam. (d) the reciprocal space mapping near the MgO and film (113) diffraction region (e) XRD 2θ-ω scan around the (002) diffraction and. (f) and (g) present STEM images of the HAADF and ABF phase, respectively. (h) the EELS in STEM at the N K edge, Ti L_{2,3} edge and O K edge from the left to right, respectively.

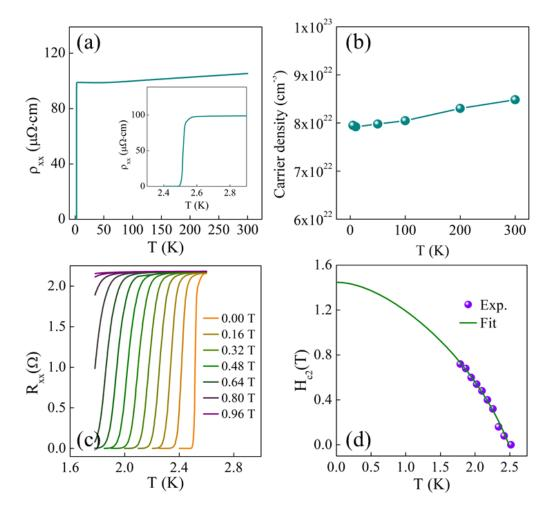


Fig. 2. Electrical transport properties of titanium oxynitride films. (a) The longitudinal resistivity of a 90 nm film as a function of temperature from 300 K to 2 K. Inset shows the superconducting transition at ~2.6 K. (b) The temperature-dependent carrier density from the transverse Hall resistivity measurement. (c) The magnetoresistance below the onset superconducting temperature. (d) The critical magnetic field as a function of temperature and the WHH model fitting (the green line).

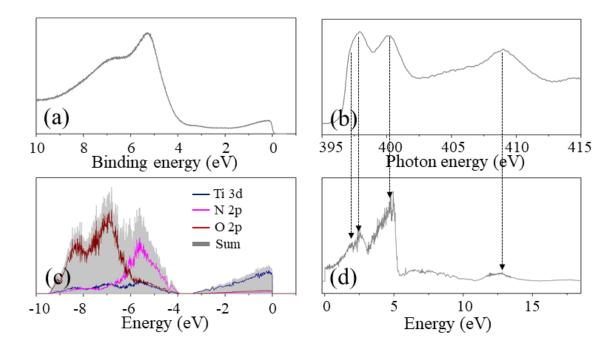


Fig. 3. Photoemission and x-ray absorption spectroscopy on Ti oxynitride films. The UPS (a) compares with the calculated spectrum from the DFT DOS weighted by the cross section of each atomic orbital (b). The XAS at the N K edge (c) and the projected p state of the N (d) from the DFT calculation using a supercell containing 64 Ti, 25 N and 39 O. The arrows are used to guide the eye for the comparison between experiment and theory. The zero of energy is at the Fermi energy in panels (a), (c) and (d).

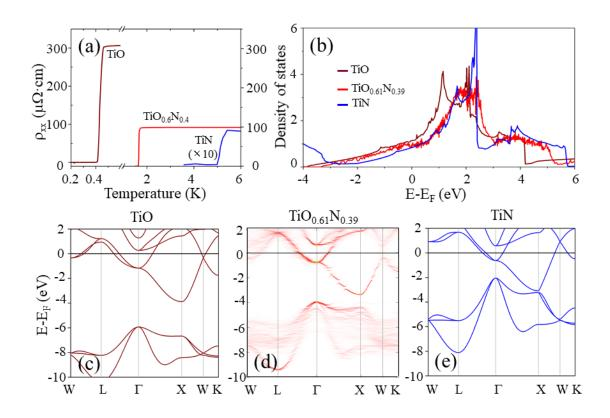


Fig. 4. The electrical transport and electronic structure properties in TiO, TiO_{0.61}N_{0.39} and TiN. (a) The low-temperature resistivity near the T_c . (b) The total density of states (unit: states/eV/TiO). (c)-(e) The low-energy band dispersion of O 2p and Ti 3d t_{2g} . The unfolded band dispersion in (d) is calculated from a Ti oxynitride supercell. The zero of energy is at the Fermi energy.

Supplementary Materials for

Critical Role of Disorder for Superconductivity in the Series of Epitaxial Ti(O,N) Films

Authors: Fengmiao Li^{1,2}, Oliver Dicks², Myung-Geun Han³, Solveig Aamlid², Giorgio Levy^{1,2}, Ronny Sutarto⁴, Chong Liu^{1,2}, Hsiang-Hsi Kung^{1,2}, Oleksandr Foyevstov^{1,2}, Simon Godin^{1,2}, Bruce A. Davidson^{1,2}, Andrea Damascelli^{1,2}, Yimei Zhu³, Christoph Heil⁵, Ilya Elfimov^{1,2}, George A. Sawatzky^{1,2}, Ke Zou^{1,2}

Affiliations:

¹Department of Physics & Astronomy, University of British Columbia, Vancouver, British Columbia, V6T 1Z1 Canada.

²Quantum Matter Institute, University of British Columbia, Vancouver, British Columbia, V6T 1Z4 Canada.

³Condensed Matter Physics & Materials Science Department, Brookhaven National Laboratory, Upton, New York, 11973 USA.

⁴Canadian Light Source, Saskatoon, Saskatchewan, S7N 2V3 Canada.

⁵Institute of Theoretical and Computational Physics, Graz University of Technology, NAWI Graz, 8010 Graz, Austria

This PDF file includes:

Figs. S1 to S4

- S1 X-ray photoemission spectroscopy on uncapped Ti oxynitride films
- S2 X-ray absorption spectroscopy on Ge-capped TiO oxynitride films
- S3 The Ti oxynitride supercell
- S4 The unfolded phonon dispersion calculated from the $Ti_{64}N_{25}O_{39}$ supercell.

Figure S1

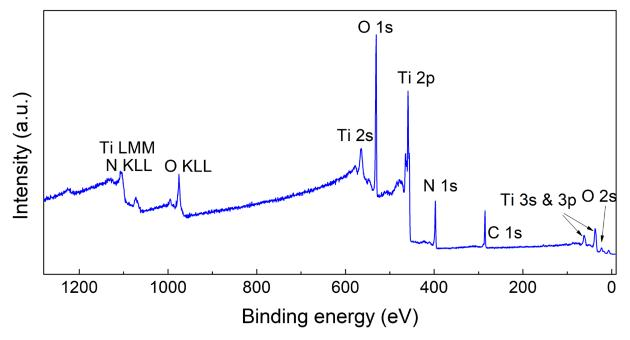


Figure. S1. X-ray photoemission spectroscopy of uncapped Ti oxynitride films. Carbon and stronger oxygen signal are seen in the spectroscopy because of the surface contamination and oxidization after air exposure.

Figure S2

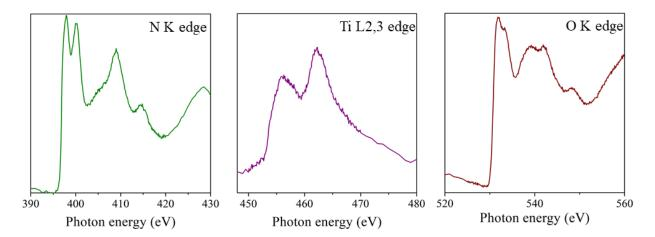


Figure S2. X-ray absorption spectroscopy (fluorescence yield mode) of Ge-capped Ti oxynitride films. From left to right: $N ext{ K edge}$, $Ti ext{ L}_{2,3}$ edge and $O ext{ K edge}$.

Figure S3

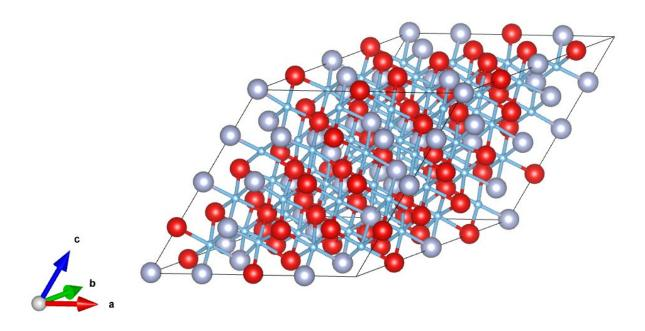


Figure S3. The relaxed atomic structure for Ti oxynitride calculations. Red: oxygen; Gray: nitrogen; Blue: titanium. The (4×4) supercell of the primitive unitcell contains 64 Ti, 39 O and 25 N, which corresponds to the chemical stoichiometry $TiO_{0.61}N_{0.39}$.

Figure S4

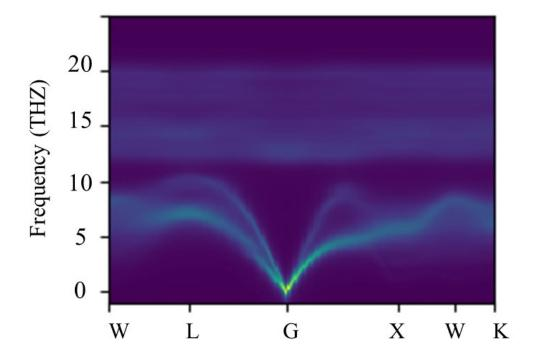


Figure S4. The unfolded phonon dispersion calculated from the $Ti_{64}N_{25}O_{39}$ supercell.